

Development of a versatile two-photon endoscope for biological imaging

Youbu Zhao,^{1,*} Hiroshi Nakamura,² and Robert J. Gordon¹

¹Department of Chemistry, University of Illinois at Chicago, Chicago, IL 60607, USA

²Department of Ophthalmology, Summa Health System, Akron, OH 44309, USA

*zhaoyoubo@gmail.com

Abstract: We describe a versatile, catheter-type two-photon probe, designed for *in vivo* and *ex vivo* imaging of the aqueous outflow pathway in the eye. The device consists of a silica double cladding fiber used for laser delivery and fluorescence collection, a spiral fiber scanner driven by a miniature piezoelectric tube, and an assembly of three micro-size doublet achromatic lenses used for focusing the laser and collecting the two-photon excitation signal. All the components have a maximum diameter of 2 mm and are enclosed in a length of 12-gauge stainless steel hypodermic tubing having an outer diameter of 2.8 mm. The lateral and axial resolutions of the probe are measured to be 1.5 μm and 9.2 μm , respectively. Different lens configurations and fibers are evaluated by comparing their spatial resolutions and fluorescence signal collection efficiencies. Doublet achromatic lenses and a double cladding fiber with a high inner cladding numerical aperture are found to produce a high signal collection efficiency, which is essential for imaging live tissues. Simple methods for reducing image distortions are demonstrated. Images of human trabecular meshwork tissue are successfully obtained with this miniature two-photon microscope.

© 2010 Optical Society of America

OCIS codes: (110.0180) Microscopy; (110.2350) Fiber optics imaging; (170.0110) Imaging systems; (170.2150) Endoscopic imaging; (180.5810) Scanning microscopy.

References and links

1. W. Denk, J. H. Strickler, and W. W. Webb, "Two-photon laser scanning fluorescence microscopy," *Science* **248**(4951), 73–76 (1990).
2. W. R. Zipfel, R. M. Williams, and W. W. Webb, "Nonlinear magic: multiphoton microscopy in the biosciences," *Nat. Biotechnol.* **21**(11), 1369–1377 (2003).
3. A. Diaspro, G. Chirico, and M. Collini, "Two-photon fluorescence excitation and related techniques in biological microscopy," *Q. Rev. Biophys.* **38**(2), 97–166 (2005).
4. L. Fu, and M. Gu, "Fibre-optic nonlinear optical microscopy and endoscopy," *J. Microsc.* **226**(3), 195–206 (2007).
5. P. Kim, M. Puoris'haag, D. Côté, C. P. Lin, and S. H. Yun, "In vivo confocal and multiphoton microendoscopy," *J. Biomed. Opt.* **13**(1), 010501 (2008).
6. K. König, A. Ehlers, I. Riemann, S. Schenkl, R. Bückle, and M. Kaatz, "Clinical two-photon microendoscopy," *Microsc. Res. Tech.* **70**(5), 398–402 (2007).
7. F. Helmchen, M. S. Fee, D. W. Tank, and W. Denk, "A miniature head-mounted two-photon microscope. high-resolution brain imaging in freely moving animals," *Neuron* **31**(6), 903–912 (2001).
8. B. A. Flusberg, E. D. Cocker, W. Piyawattanametha, J. C. Jung, E. L. M. Cheung, and M. J. Schnitzer, "Fiber-optic fluorescence imaging," *Nat. Methods* **2**(12), 941–950 (2005).
9. W. Göbel, J. N. D. Kerr, A. Nimmerjahn, and F. Helmchen, "Miniaturized two-photon microscope based on a flexible coherent fiber bundle and a gradient-index lens objective," *Opt. Lett.* **29**(21), 2521–2523 (2004).
10. J. C. Jung, A. D. Mehta, E. Aksay, R. Stepnoski, and M. J. Schnitzer, "In vivo mammalian brain imaging using one- and two-photon fluorescence microendoscopy," *J. Neurophysiol.* **92**(5), 3121–3133 (2004).
11. B. A. Flusberg, J. C. Jung, E. D. Cocker, E. P. Anderson, and M. J. Schnitzer, "In vivo brain imaging using a portable 3.9 gram two-photon fluorescence microendoscope," *Opt. Lett.* **30**(17), 2272–2274 (2005).
12. L. Fu, A. Jain, H. K. Xie, C. Cranfield, and M. Gu, "Nonlinear optical endoscopy based on a double-clad photonic crystal fiber and a MEMS mirror," *Opt. Express* **14**(3), 1027–1032 (2006).

13. M. T. Myaing, D. J. MacDonald, and X. D. Li, "Fiber-optic scanning two-photon fluorescence endoscope," *Opt. Lett.* **31**(8), 1076–1078 (2006).
14. C. J. Engelbrecht, R. S. Johnston, E. J. Seibel, and F. Helmchen, "Ultra-compact fiber-optic two-photon microscope for functional fluorescence imaging in vivo," *Opt. Express* **16**(8), 5556–5564 (2008).
15. Y. C. Wu, J. F. Xi, M. J. Cobb, and X. D. Li, "Scanning fiber-optic nonlinear endomicroscopy with miniature aspherical compound lens and multimode fiber collector," *Opt. Lett.* **34**(7), 953–955 (2009).
16. D. Bird, and M. Gu, "Compact two-photon fluorescence microscope based on a single-mode fiber coupler," *Opt. Lett.* **27**(12), 1031–1033 (2002).
17. Y. C. Wu, Y. X. Leng, J. F. Xi, and X. D. Li, "Scanning all-fiber-optic endomicroscopy system for 3D nonlinear optical imaging of biological tissues," *Opt. Express* **17**(10), 7907–7915 (2009).
18. L. Fu, X. S. Gan, and M. Gu, "Nonlinear optical microscopy based on double-clad photonic crystal fibers," *Opt. Express* **13**(14), 5528–5534 (2005).
19. L. Fu, and M. Gu, "Double-clad photonic crystal fiber coupler for compact nonlinear optical microscopy imaging," *Opt. Lett.* **31**(10), 1471–1473 (2006).
20. R. Le Harzic, I. Riemann, M. Weinigel, K. König, and B. Messerschmidt, "Rigid and high-numerical-aperture two-photon fluorescence endoscope," *Appl. Opt.* **48**(18), 3396–3400 (2009).
21. G. Binnig, and D. P. E. Smith, "Single-tube three-dimensional scanner for scanning tunneling microscopy," *Rev. Sci. Instrum.* **57**(8), 1688–1689 (1986).
22. J. C. Jung, and M. J. Schnitzer, "Multiphoton endoscopy," *Opt. Lett.* **28**(11), 902–904 (2003).
23. D. W. Piston, B. R. Masters, and W. W. Webb, "Three-dimensionally resolved NAD(P)H cellular metabolic redox imaging of the in situ cornea with two-photon excitation laser scanning microscopy," *J. Microsc.* **178**(Pt 1), 20–27 (1995).
24. M. Johnson, "What controls aqueous humour outflow resistance?" *Exp. Eye Res.* **82**(4), 545–557 (2006).
25. E. R. Tamm, "The trabecular meshwork outflow pathways: structural and functional aspects," *Exp. Eye Res.* **88**(4), 648–655 (2009).
26. H. Y. Gong, R. C. Tripathi, and B. J. Tripathi, "Morphology of the aqueous outflow pathway," *Microsc. Res. Tech.* **33**(4), 336–367 (1996).
27. A. J. Sit, F. M. Coloma, C. R. Ethier, and M. Johnson, "Factors affecting the pores of the inner wall endothelium of Schlemm's canal," *Invest. Ophthalmol. Vis. Sci.* **38**(8), 1517–1525 (1997).
28. S. Toyran, Y. M. Liu, S. Singha, S. Shan, M. R. Cho, R. J. Gordon, and D. P. Edward, "Femtosecond laser photodisruption of human trabecular meshwork: an in vitro study," *Exp. Eye Res.* **81**(3), 298–305 (2005).
29. H. Nakamura, Y. M. Liu, T. E. Witt, R. J. Gordon, and D. P. Edward, "Femtosecond laser photodisruption of primate trabecular meshwork: an ex vivo study," *Invest. Ophthalmol. Vis. Sci.* **50**(3), 1198–1204 (2008).
30. D. A. Ammar, T. C. Lei, E. A. Gibson, and M. Y. Kahook, "Two-photon imaging of the trabecular meshwork," *Mol. Vis.* **16**, 935–944 (2010).
31. D. C. Leiner, and R. Prescott, "Correction of chromatic aberrations in GRIN endoscopes," *Appl. Opt.* **22**(3), 383–386 (1983).
32. X. M. Liu, M. J. Cobb, Y. C. Chen, M. B. Kimmey, and X. D. Li, "Rapid-scanning forward-imaging miniature endoscope for real-time optical coherence tomography," *Opt. Lett.* **29**(15), 1763–1765 (2004).
33. M. W. Davidson, and M. Abramowitz, "Optical microscopy," in *Encyclopedia of imaging science and technology*, J. P. Hornak, (J. Wiley, New York, 2002).
34. Y. Sako, A. Sekihata, Y. Yanagisawa, M. Yamamoto, Y. Shimada, K. Ozaki, and A. Kusumi, "Comparison of two-photon excitation laser scanning microscopy with UV-confocal laser scanning microscopy in three-dimensional calcium imaging using the fluorescence indicator Indo-1," *J. Microsc.* **185**(1), 9–20 (1997).
35. M. Gu, and D. Bird, "Three-dimensional optical-transfer-function analysis of fiber-optical two-photon fluorescence microscopy," *J. Opt. Soc. Am. A* **20**(5), 941–947 (2003).
36. K. Tanaka, N. Saga, and K. Hauchi, "Focusing of a Gaussian beam through a finite aperture lens," *Appl. Opt.* **24**(8), 1098–1101 (1985).
37. L. Fu, X. S. Gan, and M. Gu, "Characterization of gradient-index lens-fiber spacing toward applications in two-photon fluorescence endoscopy," *Appl. Opt.* **44**(34), 7270–7274 (2005).
38. K. Nishizawa, "Chromatic aberration of the Selfoc lens as an imaging system," *Appl. Opt.* **19**(7), 1052–1055 (1980).
39. M. T. Myaing, J. Y. Ye, T. B. Norris, T. Thomas, J. R. Baker, Jr., W. J. Wadsworth, G. Bouwmans, J. C. Knight, and P. S. J. Russell, "Enhanced two-photon biosensing with double-clad photonic crystal fibers," *Opt. Lett.* **28**(14), 1224–1226 (2003).
40. Y. C. Chang, J. Y. Ye, T. Thomas, Y. Chen, J. R. Baker, and T. B. Norris, "Two-photon fluorescence correlation spectroscopy through a dual-clad optical fiber," *Opt. Express* **16**(17), 12640–12649 (2008).
41. F. Helmchen, D. W. Tank, and W. Denk, "Enhanced two-photon excitation through optical fiber by single-mode propagation in a large core," *Appl. Opt.* **41**(15), 2930–2934 (2002).
42. C. M. Brown, P. G. Reinhall, S. Karasawa, and E. J. Seibel, "Optomechanical design and fabrication of resonant microscanners for a scanning fiber endoscope," *Opt. Eng.* **45**(4), 043001 (2006).
43. S. Lemire-Renaud, M. Rivard, M. Strupler, D. Morneau, F. Verpillat, X. Daxhelet, N. Godbout, and C. Boudoux, "Double-clad fiber coupler for endoscopy," *Opt. Express* **18**(10), 9755–9764 (2010).
44. A. M. Weiner, "Femtosecond pulse shaping using spatial light modulators," *Rev. Sci. Instrum.* **71**(5), 1929–1960 (2000).

45. P. Xi, Y. Andegeko, D. Pestov, V. V. Lovozoy, and M. Dantus, "Two-photon imaging using adaptive phase compensated ultrashort laser pulses," *J. Biomed. Opt.* **14**(1), 014002 (2009).
 46. B. von Vacano, T. Buckup, and M. Motzkus, "In situ broadband pulse compression for multiphoton microscopy using a shaper-assisted collinear SPIDER," *Opt. Lett.* **31**(8), 1154–1156 (2006).
-

1. Introduction

Two-photon (2P) excitation microscopy has opened up new avenues for biomedical investigations in living tissues [1,2]. Superior properties of 2P microscopy, including intrinsic sectioning ability that obviates the need for a confocal pinhole, increased penetration depth in light-scattering media through the use of a longer wavelength (red or infrared) excitation laser, and reduced out-of-focus photobleaching, make it an indispensable tool for high-resolution imaging of structures in thick tissues and in live animals. Although many applications have been reported using bulky, bench-top 2P microscopes to image outer tissue layers [3], there is a clear need for a miniaturized and flexible 2P endoscope that would allow imaging of inner organs [4–7]. Driven by this need, 2P endoscopy has advanced rapidly, benefiting from improvements in optical fibers and micro-optical and micro-mechanical components [6,8].

Many advances in 2P endoscopy have been reported in the last decade [9–14]. Most endoscope designs involve three key components: micro-optics used for imaging, optical fibers used for efficient laser delivery and signal collection, and miniaturized scanning devices. The micro-sized imaging optics usually consist of either gradient-index (GRIN) lenses or compound lenses [15]. Several types of optical fibers have been used for construction of endoscopes, including single mode fibers [16], conventional double cladding fibers [13,17], photonic crystal fibers (PCFs) [12,18,19], and two-fiber systems consisting of one hollow core PCF for laser delivery and another multimode fiber for fluorescence signal collection [14,20]. The two prevailing choices for the scanning unit are microelectromechanical systems (MEMS) based on small scanning mirrors [12] and mechanically scanned fiber cantilevers driven by a piezoelectric transducer (PZT) [13,21]. Some endoscopes avoid introducing a compact scanner by using long cylindrical GRIN relay lenses [6,22] or a coherent fiber bundle [9] to project the laser focus. With these designs, the laser focus is scanned by bulky components located outside of the endoscope, at the cost of flexibility and resolution. Among the various designs, light-weight and catheter-like 2P endoscopes employing PZT-driven fiber cantilever scanners and GRIN lenses have been demonstrated to be advantageous over other endoscopy technologies in terms of size, weight, and flexibility [4,13,14,19]. Despite these advances, few clinical or biological applications of 2P endoscopes for tissue imaging have been reported [14,17], largely because of the challenges of efficient fluorescence signal collection [15]. Especially for applications involving intrinsically weak autofluorescence signals, as, for example, from NADH [23], the signal-to-noise level of fiber-based endoscopy is still far from satisfactory.

Here we report the design and construction of a miniaturized, fiber-based 2P endoscope, intended for real-time imaging of the aqueous outflow pathway, including the trabecular meshwork (TM) in the eye. The TM is the primary site for regulation of the normal bulk flow of the aqueous humor [24,25]. Abnormalities in the structure and function of the aqueous outflow pathway, including the TM, are considered to be one of the major reasons for elevated intraocular pressure in primary angle open glaucoma [24]. A real-time imaging tool is needed in this field because conventional histological methods are plagued with artifacts introduced during the tissue-fixing procedure that have led to confusion and debate in the ophthalmological literature [26,27]. Recently, 2P microscopy has been shown to be a promising tool for investigating the structure and function of the aqueous outflow pathway [28–30]. Using this approach to image living eye tissues with commercially available 2P microscopes is impractical, however, because such instruments require the subject to be immobilized and affixed to a glass slide mounted on the microscope stage [30]. The flexibility

of a compact catheter-type 2P probe promises to overcome these obstacles by allowing *ab interno* imaging of the eye.

In order to explore the feasibility of employing 2P endoscopy for *ex vivo* study of the aqueous outflow pathway using an anterior segment perfusion culture system of the eye, we constructed a light-weight, catheter-like microscope and demonstrated its capability for imaging human TM. The miniaturized microscope consists of a PZT-driven resonant fiber scanner, a silica double cladding fiber, and three doublet achromatic lenses. Different lens configuration and fiber options were investigated during the construction of the instrument in order to obtain good spatial resolution and high fluorescence collection efficiency. Doublet achromatic lenses and a double cladding fiber were chosen for the instrument primarily to enhance its fluorescence signal collection efficiency, as compared with that obtained with other 2P microscopes [13,14,17]. In particular, three achromatic doublet lenses were used instead of GRIN lenses to reduce achromatic aberration [31]. A silica double cladding fiber with a high numerical aperture (NA) in the inner cladding was selected to optimize the balance among the signal collection efficiency, imaging resolution, and autofluorescence background inside the fiber. Simple methods are demonstrated in this paper to reduce image distortions that are inherent with resonant fiber scanner imaging modalities. Optimization of the signal to noise level enabled us to obtain good 2P images of human TM tissue, thereby laying the foundation for further *ex vivo* or *in vivo* investigation of the aqueous humor outflow pathway.

This paper is organized as follows. Details of the instrument design are presented in the following section. The performance of its various components and the motivation behind their design are discussed in Section 3. Section 4 presents the application of the endoscope to imaging of the TM tissue *in vitro*. Suggestions for future improvements and a summary are presented in the final two sections.

2. Instrument Design

The overall design of the 2P endoscope is illustrated schematically in Fig. 1(a). Ultrashort 35 fs, 800 nm laser pulses, generated from a commercial mode-locked Ti:Sapphire oscillator (Tsunami, Spectra Physics), are steered by a 45° dichroic mirror (650dcspxr, Chroma) and coupled into the core of a 1.1 m long double cladding optical fiber (P-6/125DC, Liekki) by a 0.4 NA objective (M-20X, Newport) and then focused at the image plane by an assembly of three miniature doublet achromatic lenses having diameters of 2 mm (one component of NT65-569, $f = 6$ mm, and two components of NT65-567, $f = 3$ mm, Edmund Optics). Before the dichroic mirror, the laser pulses pass through a grating pair (600 lines/mm, Newport) to pre-compensate for dispersion introduced by the fiber, which we estimate to be approximately $37,000 \text{ fs}^2$. Fluorescence emitted from the sample mounted on a 3D translation stage (462-XYZ-SD, Newport) is collected in the backwards direction by the same lenses and coupled into the inner cladding and core of the fiber. After passing through the dichroic mirror and a short pass filter (E700SP, Chroma), the fluorescence signal is detected by a photomultiplier tube (PMT, H7422P, Hamamatsu) and digitized by a data acquisition card (PCI6115, National Instruments). Scanning of the laser focus is achieved by moving the distal tip of the fiber, which was driven by a custom-designed piezoelectric actuator (1.5 mm of outer diameter, Physik Instrumente). The piezoelectric transducer holding the fiber and focusing lenses is enclosed in a 25 mm length of stainless steel 12-gauge hypodermic-needle tubing having an outer diameter of 2.8 mm. The working distance of the probe is 420 μm . A photograph of the assembled probe is shown in Fig. 1(d).

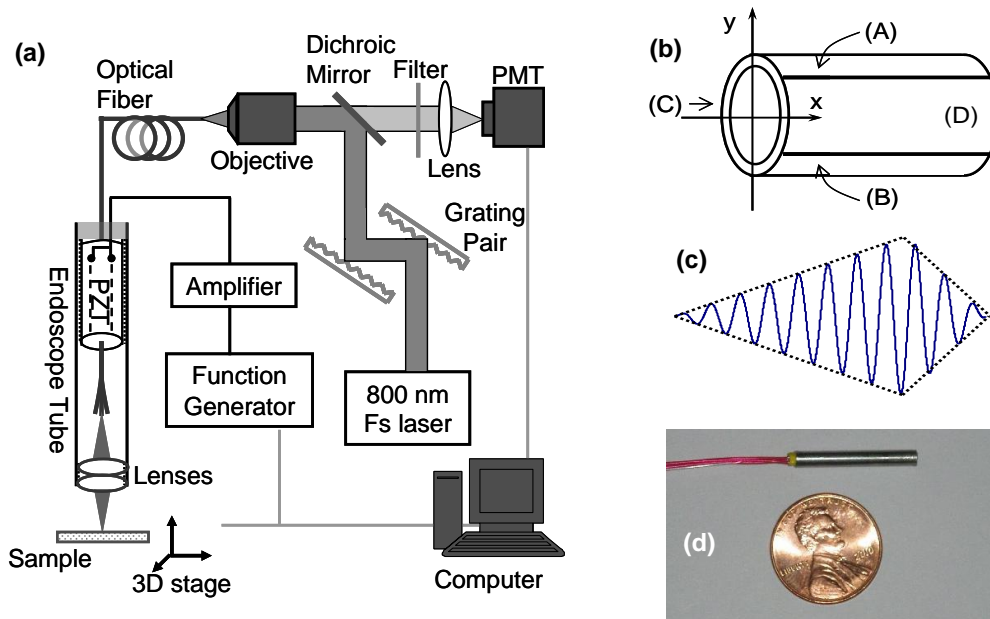


Fig. 1. Schematic setup of the two-photon excitation fluorescence endoscope (a), structure of the piezoelectric actuator (b), drive waveform for a spiral scan of the fiber distal tip (c), and photograph of the assembled 2P microscope probe (d).

The outer surface of the PZT is divided into four equal strips, each connected to an electrode [Fig. 1(b)] [21], with the inner surface of the PZT serving as a common ground. The actuator is deflected along either the y - or x -axis when a voltage is applied across the corresponding pair of electrodes (A-B or C-D), with one electrode in each pair having a positive voltage and the other a negative voltage. The quadrant segment design enables the actuator to be deflected in two orthogonal directions (x and y). The fiber is threaded through and attached to the PZT with a 10 mm long cantilever arm starting from the end of the PZT. Scanning of the fiber is realized by deflecting the PZT at the mechanical resonant frequency of the distal tip of the fiber, typically 820 Hz in the present setup. Cyclic scanning is generated by applying two sinusoidal voltage wave forms with a nominally 90° degree phase lag between the two channels of the actuator.

To obtain two dimensional images, expanding spiral scanning patterns are imposed on the fiber cantilever by using sinusoidal driving voltages with linearly varying amplitudes, which are generated by an arbitrary function generator (AFG3022B, Tektronics) and amplified by piezo driver modules (E-835, Physik Instrumente). Because the function generator has only two channels, a two-channel voltage-inverting operational amplifier was built to provide additional drive signals of opposite sign. Two in-phase waveforms of opposite sign were used as the drive signals for each channel of the PZT. The voltage pair for each channel is provided by the original output of one channel of the function generator and its inverted waveform generated by the operational amplifier. The driving waveforms are shown in Fig. 1(c). The first half cycle of the driving waveform is used to generate expanding cycles for construction of a frame image with 200×200 pixels. The second half of the waveform is used to reset and settle the fiber and to provide the time needed for data acquisition. The diameter of the scanning pattern of the fiber distal tip, which determined the field of view of the images, is controlled by varying the amplitude of the driving voltage. The frame rate, which is determined by the resonant frequency of the fiber distal tip, is 1.1 frames/second for the instrument reported here. Although the imaging speed can be increased easily by using a shorter fiber cantilever, thereby increasing the resonant frequency [32], we prefer this low

speed because of the decreased signal/noise ratio at higher scan rates. A home-developed computer interface is used for fiber scanning, signal detection, and image display.

3. Design Criteria and Performance of the Endoscope

3.1. Focusing Optics

As a key component of the endoscope, the imaging optics focus the laser beam onto the object and collect the resulting fluorescence. The focal length, NA, and optical aberration of the lenses determine the resolution and fluorescence collection efficiency of the probe. While constructing the endoscope, we tested three types of micro-lenses, namely GRIN, aspherical, and doublet achromatic lenses (and combinations of these lenses), all of which were obtained commercially. Specifically, we tested the following configurations: (i) a single GRIN lens (LGI630-2, 0.25 pitch, Newport), (ii), an aspheric lens (354430-A, 0.15 NA, Thorlabs) plus a GRIN lens (LGI630-1, 0.23 pitch, Newport), and (iii) a combination of three achromatic doublet lenses (Edmund Optics). The schematic setups for the three lens configurations are shown in Fig. 2(a), 2(b) and 2(c), respectively. Comparing the performance of the instrument using these lenses, we found that an assembly of three achromatic lenses gives the best resolution and signal collection efficiency. The lenses have focal lengths of 6, 3, and 3 mm and a common diameter of 2 mm. The 6 mm focal length lens, with its convex surface facing the fiber output, serves as a collimator to transform the diverging laser beam into a parallel one. The distance between the fiber tip and the lens is approx. 6 mm, which matches the focal length of the lens. The two 3 mm lenses are mounted with their flat surfaces pressed against each other. This combination of two lenses functions as an objective to focus the collimated laser beam. The single lens collimator and double lens objective comprise an infinite conjugate optical imaging configuration [33]. In this case, the distance between the 6 mm lens and the 3 mm lens pair was adjustable, allowing the length of the probe to be adapted to specific applications. In our current instrument, with which the images reported here were obtained, this distance is 1 mm. Although GRIN and micro-aspherical lenses with higher NAs can provide better resolution, as shown in the following sections, their severe chromatic effects make them less suitable for a 2P endoscope [15,31], especially when used for live tissue applications having a weak autofluorescence signal.

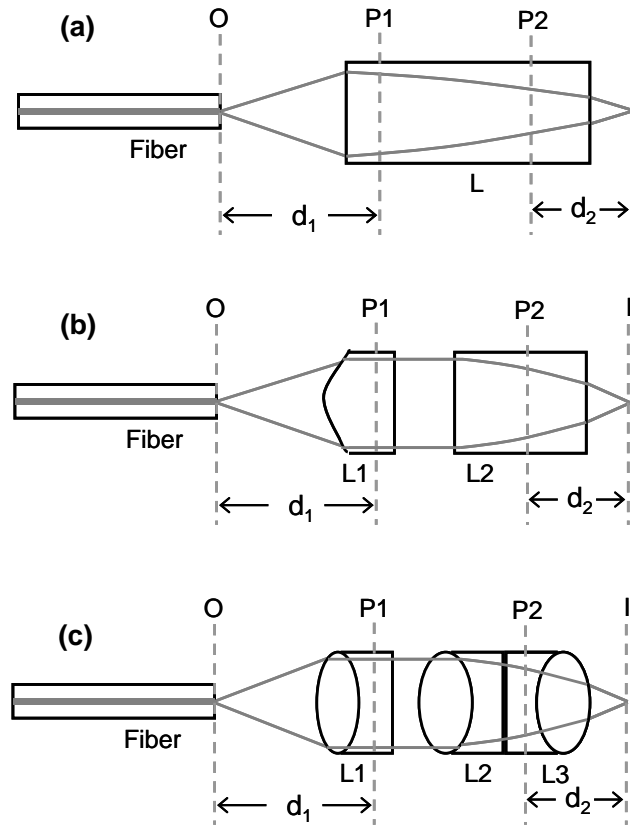


Fig. 2. ; Schematic drawing of the three lens configurations. O: Objective plane (fiber end surface); P1: objective principle plane; P2: image principle plane; I: image plane. (a), L: 0.25 pitch GRIN lens; (b), L1: 0.15 NA aspheric lens, L2: 0.23 pitch GRIN lens; (c), L1: doublet lens with focal length of 6 mm; L2, L3: doublet lenses with focal length of 3 mm.

3.2. Resolution and Field of View

The resolution of a microscope is defined as the full width at half maximum (FWHM) of the point spread function (PSF) [34]. Since the excitation probability for 2P fluorescence varies quadratically with the illuminating intensity, the PSF of the 2P probe also varies as the square of the laser intensity distribution. The latter is determined by a convolution of the fiber output laser intensity distribution and the impulse response of the focusing optics [35]. The present instrument has a non-confocal detection geometry because most of the fluorescence signal is collected by the inner cladding of the fiber. The diameter of the inner cladding is more than one order of magnitude larger than the fiber core, allowing it to be treated approximately as an infinite size detector. For simplicity, we approximate the laser intensity distribution at the focus as a Gaussian-Lorentzian spatial profile with widths ω_0 and z_0 in the radial and axial dimensions, respectively, assuming the laser output from the fiber core is a TEM₀₀ mode Gaussian beam [36], and without considering the diffraction effects of the finite aperture size of the lenses. (More rigorous calculations presented below justify this model.) Based on these approximations, the diameter of laser focus, D_l , after transformation by the focusing lenses, is given by

$$D_l = MD_{fc}, \quad (1)$$

where D_{fc} is the diameter of the fiber core, and M is the magnification ratio of the imaging lenses. The core diameter is taken to be the approximate mode-field diameter of the fiber.

Here and in throughout the paper the refractive index of air is assumed. Based on the paraxial approximation, the magnification of an imaging system is given by $M = d_2 / d_1$, where d_1 and d_2 are the distances from the object plane to the object principle plane and from the image plane to the image principle plane, respectively. In the case of our three doublet lenses, shown in Fig. 2(c), the object plane is the fiber output surface (its distal tip), and the image plane is the focal plane. Considering the infinite conjugate configuration of the focusing lenses, the magnification of the instrument is given by [33]

$$M = f_2 / f_1, \quad (2)$$

where $f_1 = 6$ mm is the focal length of the collimator, and f_2 is the effective focal length of the objective consisting of the two 3 mm lenses, calculated to be 2.6 mm. Based on this information, we find that the calculated waist ω_0 of the laser focus is 1.3 μm . For a Gaussian distribution, the FWHM of the focus is given by $[2\ln(2)]^{1/2} \omega_0$, which equals 1.5 μm .

Theoretically, the FWHM for 2P excitation is $2^{-1/2}$ times the laser FWHM. The calculated lateral resolution is therefore 1.1 μm , and the calculated axial resolution is 8.3 μm . Using the same analysis, the lateral resolutions of the other two lens configurations are 1.1 μm for the single GRIN lens [Fig. 2(a)] and 0.83 μm for the aspheric lens plus GRIN lens combination [Fig. 2(b)]. The magnification ratio of the single GRIN lens setup is 0.43, the same as for the three doublet lenses configuration, with the objective distance d_1 set at 6.2 mm. The magnification ratio may be decreased so as to increase the resolution with this configuration [13]. Doing so, however, will decrease the fluorescence collection efficiency significantly, as shown by ref. 37 and our calculation. The magnification ratio of the aspheric lens plus GRIN lens, configured as an infinite conjugate setup, is 0.33.

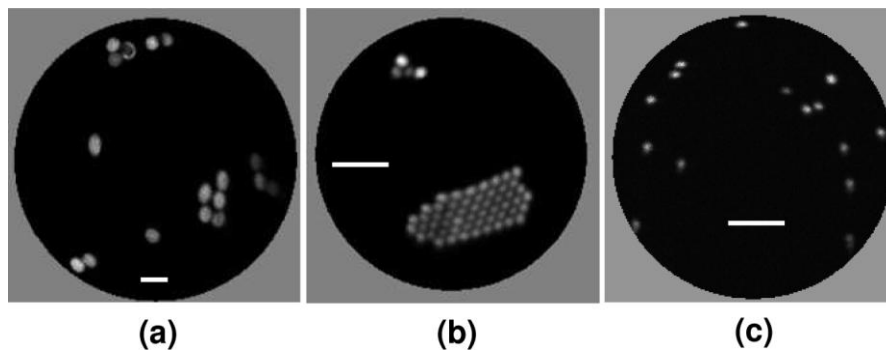


Fig. 3. Two-photon images of fluorescent spheres with diameters of 10 μm (a), 3.0-3.4 μm (b), and 1 μm (c), obtained with the endoscope. Scale bars are 20 μm .

The resolution of the endoscope was measured by imaging layers of fluorescent microbeads randomly deposited onto the surface of a microscope slide. Figure 3 shows images for several different diameter beads. Figure 4 shows the measured fluorescent intensity distribution in (a) the lateral direction for a 0.5 μm diameter bead and (b) the axial direction for a 1 μm diameter bead. Gaussian fits to the data show that the FWHMs of the intensity profiles are 1.5 μm and 9.2 μm in the lateral and axial directions, respectively. Because the sizes of the beads are much smaller than the measured FWHM in each direction, these numbers may be considered to be the actual resolutions of the system.

The PSFs of the system and convolutions of the bead fluorescence were evaluated numerically using the theoretical diffraction field for a Gaussian beam focused by a finite aperture lens [36]. The results, plotted in Fig. 4, give FWHM values of 9.1 μm and 1.2 μm in the axial and radial directions, respectively, in good agreement with our simple model. The deviations between the measurements and calculations may be due to optical aberrations of the lenses and the imperfect mode of the fiber, which were not included in the calculation.

Although the resolutions are a little poorer than those of bench-top 2P microscopes with large NA objectives, they are still sufficient to resolve structures of the TM, as shown later in this paper.

The diameter of the field of view (FOV) of the endoscope is given by

$$D_{FOV} = MD_{scan}, \quad (3)$$

where M is given by Eq. (2), and D_{scan} is the diameter of the largest spiral scan trajectory. Equations (1)–(3) show that there is a tradeoff between resolution and FOV. Considering these two competing properties of the instrument, we found a magnification ratio in the range of 0.3–0.5 to be acceptable. With the current magnification of 0.43, we obtain a FOV of 150 μm . Although larger values of the FOV may be obtained by increasing D_{scan} , we observed that the signal intensity is greatly reduced at the outer part of the image for a FOV larger than 150 μm . When the FOV is smaller than 150 μm , we found the signal intensity drops proportionally to the distance from the center, which can be explained by the faster linear velocity at the periphery than at the center. This effect was confirmed by translating a known object across the field of view. However, the faster decrease in signal intensity for a FOV >150 μm could be the result of a restricted clear aperture of the micro-lenses.

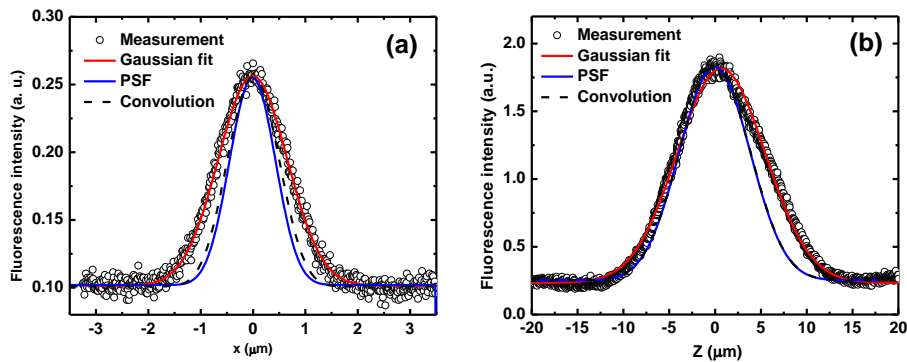


Fig. 4. Fluorescence intensity distributions (open circles) of a 1 μm fluorescent bead along the x (panel a) and z (panel b) directions, measured with the endoscope. The full width at half maximum (FWHM) values of the fitted Gaussian curves (solid red traces passing through the points) are 1.5 μm and 9.2 μm , which indicate the lateral and axial resolutions of the system, respectively. The computed point spread functions (solid blue curves), and the convolutions (black dashes) of the point spread functions and the beads profiles show the theoretical simulations.

3.3. Fluorescence Signal Collection Efficiency

As has been experienced by several other researchers, the fluorescence signal collection efficiency is a challenging problem for fiber-based endoscopes, depending strongly on the parameters of the fiber and focusing lens [13,15,19]. GRIN lenses are generally used in endoscopes because of their compact size and high NA. Chromatic aberration of GRIN lenses is a serious problem [15,31], however, that is exacerbated in 2P imaging, where the wavelength difference between the fluorescence and the excitation laser is much larger than for linear excitation. A systematic study of this problem showed that the fluorescence collection efficiency of a single GRIN lens system can vary several-fold, depending on the optical arrangement and effective NA of the lens [37]. Moreover, this study found that increasing the resolution of the system degraded the collection efficiency even further. In another study, Wu et al. [15] replaced the GRIN lens with a compound lens. Using a delicate

multimode fiber collector, they obtained an order of magnitude improvement of the collection efficiency by compensating for chromatic losses of the lenses.

In our experiments, we explored the possibility of using doublet achromatic lenses, each of which consists of two optical components cemented together to compensate for on-axis spherical and chromatic aberrations. We found that the fluorescence signal level could be increased by 6-20 times as compared to the performance of a single GRIN lens by using an assembly of three achromatic doublet lenses. To investigate the chromatic effects of different lenses, we calculated the focal shift and the resulting decrease in fluorescence detection efficiency as functions of wavelength. (The focal shift is defined with respect to the fiber tip, which lies at the geometric focus of the laser.) The results are shown in Fig. 5. In these calculations, the change in focal length caused by chromatic aberration of the lenses was obtained using thin lens equation for conventional lenses and Eq. (9) in [38] for GRIN lenses. Here we took the inner cladding diameter of the fiber as 100 μm for all three cases. These calculations show that there is a negligible loss of fluorescence collection efficiency for the three doublet lens configuration, whereas the other two configurations suffer severe chromatic losses.

The absolute fluorescence collection efficiency of the three doublet lens configuration is approx. 5%, ignoring chromatic effects and losses from the optical elements and the fiber. Although high NA (>0.3) micro-size doublet lenses, such as the 2 mm diameter ones used in our work, could be difficult to manufacture as a single element, an assembly of two or three of these lenses can provide sufficient resolution, as shown by our results. In summary, in addition to the multimode collector splicing method [15], use of doublet achromatic lenses is shown to be a good choice for improving the signal collection efficiency in 2P excitation endoscopy.

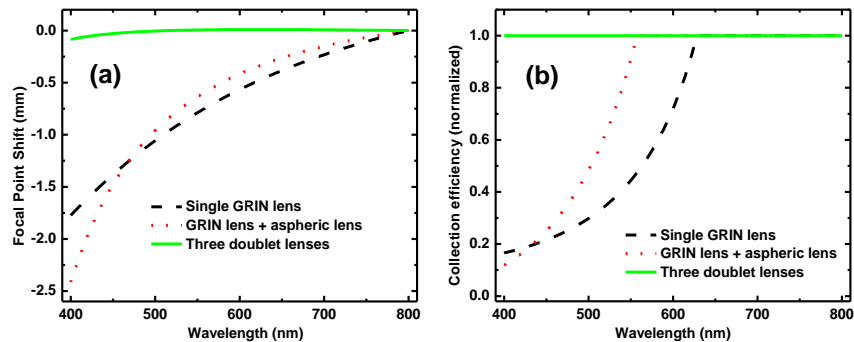


Fig. 5. Calculated chromatic effects of different lens configurations: (a) shift in the focal point with respect to the fiber tip and (b) change in the fluorescence collection efficiency as functions of fluorescence wavelength. The solid, dashed, and dotted curves correspond to the three doublet lens, single GRIN lens, and GRIN + aspheric lens configurations, respectively.

3.4. Selection of the Fiber

Selection of an appropriate fiber, which is responsible for laser delivery and fluorescence signal collection, is of great importance in the design of miniature endoscopes. Several types of fibers have been reported as options for the construction of an endoscope [4], including single mode (conventional or large mode) fibers [16], silica double cladding fibers [13], and photonic crystal fibers [19]. Among them, the single mode fiber has been proven to be the least efficient in terms of fluorescence signal collection because of its low NA and small mode field diameter [39], although it does provide the best imaging resolution [16]. The situation is even worse for 2P excitation, where achromatic effects are much stronger because of the large difference between the excitation and fluorescence wavelengths. Consequently, the single mode fiber is not a good choice for single fiber 2P endoscopy, especially for application to

tissue imaging, where high fluorescence collection efficiency is required. A hollow-core single mode PCF is frequently mentioned as an ideal option for high-power, ultrashort pulse delivery, but it cannot be used in a single-fiber-based endoscope to facilitate simultaneous pulse delivery and backward signal collection because of its narrow bandwidth (typically only tens of nanometers), unless a second fiber is employed in parallel for signal collection [4,14].

Table 1. Comparison of the parameters of different double cladding fibers

Fibers	Core diameter	Core NA	Inner clad diameter	Inner clad NA
P6/125DC	5.5 ± 0.5	0.15 ± 0.01	125 ± 2	>0.46
P10/125DC	10 ± 1	0.08 ± 0.01	125 ± 2	>0.46
SMM900	4.0 ± 0.5	0.19 ± 0.1	102 ± 2	0.26 ± 0.02
DC-165-16	16 ± 2	0.04	163 ± 5	0.61 ± 0.05

Double cladding fibers based on either ion doped silica or photonic structures, consisting of a single mode core (for laser delivery) and a multimode inner cladding (for fluorescence collection), have been employed to increase the collection efficiency by one to two orders of magnitude, while providing resolution comparable to that of a single mode fiber [13,18,39]. In our experiments, we tested four types of double clad fibers, namely the P6/125DC, P10/125DC (both from Liekki), the SMM900 (Fibercore), and a photonic crystal fiber (DC-165-16, Crystal Fibre A/S1). The physical properties of these fibers are listed in Table 1. We found that the DC-165-16 gave the best signal collection efficiency, while the others had smaller, comparable efficiencies. Geometrically, the fluorescence collection efficiency is proportional to the ratio of the diameter of the inner cladding to the beam diameter at the fiber tip, provided that the divergence of the beam is smaller than the NA of the inner cladding, which is the case of our experiments. The higher collection efficiency of the PCF is readily attributable to its larger inner cladding diameter and higher NA, as compared to the other three silica fibers. In terms of resolution, however, the PCF gave the poorest performance because it has the largest core diameter. The dependence of resolution on fiber core diameter is described by Eq. (1). Balancing the tradeoff between resolution and collection efficiency, we found the P6/125DC to be the optimum fiber for 2P excitation endoscopy. Although another option, the P4/126DC fiber, could provide better resolution than the P6/125DC, its autofluorescence background is problematic [40]. A similar problem was manifested with the SM900 fiber. In terms of resolution, the large core single mode fibers are also poor choices for 2P excitation endoscopy [41].

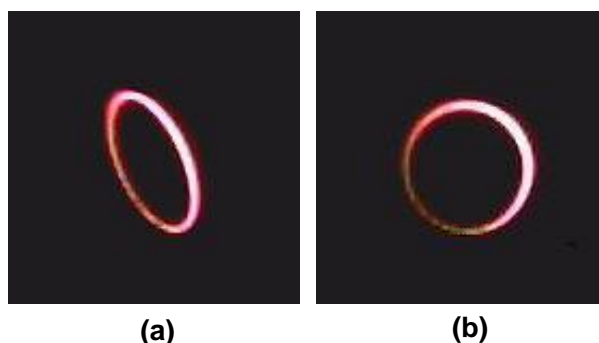


Fig. 6. Scanning pattern of the laser focus obtained by applying constant amplitude sinusoidal waveforms to the two channels of the PZT. The relative phases between the two drive signals are (a) 90° and (b) 50° .

3.5. Fiber Scanning and Suppression of Image Distortion

As mentioned previously, the compact, simple and inexpensive, resonant fiber scanner is a promising option for construction of flexible 2P endoscopes. A drawback of this method,

however, is distortions in images obtained with a resonant scanning fiber, which must be treated carefully [13,14]. The main distortions are stretching of the image and swelling of the center of the image caused by deviations between the actual fiber motion and the predicted trajectory defined by the driving signals [14]. The resonant properties of the fiber cantilever are a major source of these deviations. For example, the resonant frequencies of the two orthogonal channels differ because of the inhomogeneous geometry of the fiber, which produces a cylindrical scan when driven by equal voltages in the two channels, as shown in Fig. 6(a) [14]. This effect stretches the images. Two methods have been proposed to overcome this problem. One approach is to track the trajectory of the scanning fiber with a position-sensitive detector to create a look-up table [LUT], which is used to remap the pixel positions and correct for the distortions [14]. The other method is to modify the geometry of the fiber surface by means of selective etching to adjust the mechanical properties of the fiber cantilever [42].

Considering the complexities in applying either of these two methods, we explored the feasibility of reducing image stretching by simply controlling the drive signals. As shown by our experiments (Fig. 6), the elliptical scan orbit can be corrected to a circular trajectory by altering the driving voltages or the relative phases between the two channels. In practice we found changing the phase to be the better choice, because varying the voltages (i.e., decreasing the relative voltage of one of the two channels) decreases the maximum fiber deflection. In the endoscope setup reported here, the relative phase lag between the two channels was adjusted to 50° instead of the expected 90° quadrature. With this simple method, image stretching was mostly eliminated, as shown by the bead images in Figs. 3 and 7(b). A slight distortion is still discernable, which could be caused by the remaining deviations at different drive amplitudes. The residual distortion might possibly be removed by applying a time-varying phase lag between the two channels.

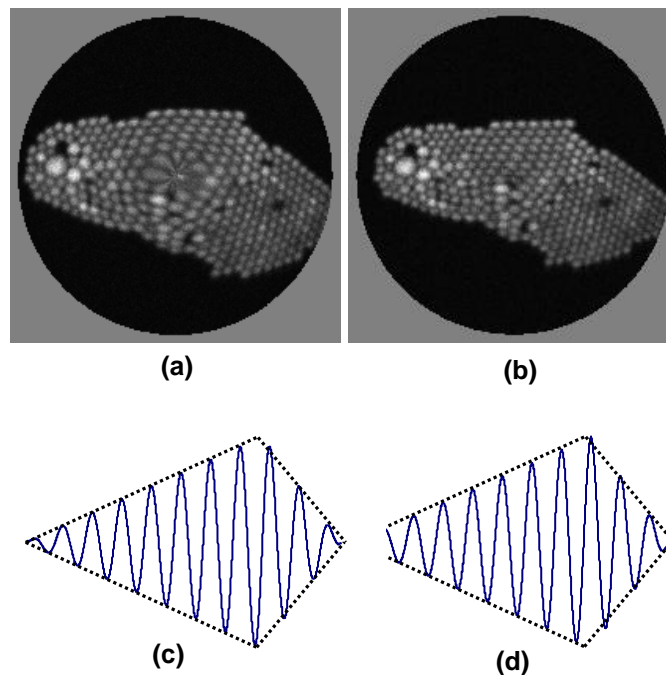


Fig. 7. Two-photon images of $3.0\text{-}3.4\ \mu\text{m}$ fluorescent beads obtained with the endoscope before (a) and after (b) removal of the center distortions. (c) and (d) are the waveforms used to drive the PZT to generate images (a) and (b), respectively.

Another type of distortion encountered in our experiments is a swelling near the center of the image, shown in Fig. 7(a). This effect is caused by a large deviation of the fiber motion from the trajectory defined by the drive signal below or near a threshold drive voltage. We are referring here to the threshold drive voltage of the PZT needed to excite the resonant vibration of the fiber distal tip. The center swelling was removed by increasing the threshold driving voltage to 1.5 V, as shown Figs. 7(b) and 7(d). By shifting the position of the sample and comparing the corresponding images (in this case, the areas of interest are at different locations within the field of view of the images), we found that no information is lost near the central area after applying this nonzero starting drive signal.

4. Imaging of the Trabecular Meshwork

Corneoscleral rims including the TM were obtained from donor eyes and fixed with 10% buffered formalin. After rinsing with phosphate buffered saline, the tissue was treated with 4'-6-diamidino-2-phenylindole (DAPI, Invitrogen) for nuclear staining. Averages of 50 images were taken because of the low signal to noise ratio (~3:1), at a laser power of 20 ± 10 mW. The large error bar is due to uncertainty in the determination of the optimum laser profile when an iris is used to block the laser output from the inner cladding [18]. Trabecular beams and cell nuclei are clearly visible, and different tissue structures of the TM, such as the uveal and corneoscleral meshwork, are well resolved with our miniature 2P endoscope (Fig. 8). A consequence of using only short pass filters in the system is that the signal generated from the trabecular beams is a combination of autofluorescence of NADH and second harmonic generation (SHG) from collagen beams [30]. The SHG signal is not as strong as might be expected, however, because of the low transmittances of the dichroic mirror and SP filter at 400 nm (60% and 20%, respectively).

These images indicate that, after improvement in resolution and signal collection efficiency, real-time investigation for the structure and function of the aqueous outflow pathway in the eye is feasible with our 2P endoscope.

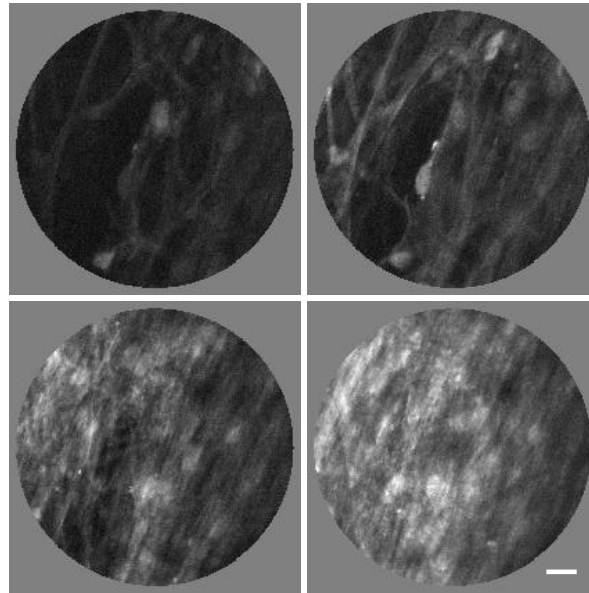


Fig. 8. Two-photon endoscopic images from a sequence of human TM z-sections. The depth interval of successive images is $20 \mu\text{m}$. Scale bars are $20 \mu\text{m}$. Top images show irregularly arranged strands in the uveal meshwork, and bottom images display flat and interacting beams or plates in the corneoscleral meshwork. Nuclei of TM cells were stained with DAPI.

5. Future Improvements

Several techniques could be employed in the future to further improve the endoscope system, including a LUT to remove image distortion [14], a fiber coupler to improve the laser delivery [19,43], active dispersion compensation to obtain the shortest possible pulse duration at the target [44], and better design of the focal lenses. In particular, an active pulse shaping method to compensate for dispersion by the optical components in order to obtain a transform-limited pulse width at the laser focal position, which has already been applied to bench-top 2P microscopy [45,46], could be employed for endoscopes to increase the signal level and image contrast. With the improved signal levels achievable with the above-mentioned techniques, the imaging speed could be increased by increasing the resonant frequency of the scanner, using a short length fiber cantilever [13]. Additional improvement might be achieved by better coupling of the laser pulses into the fiber. It has been reported that coupling the laser into the core of a double cladding fiber inevitably introduces some propagating modes in the inner cladding [18]. The fraction of the laser energy penetrating the inner cladding depends on the design of the coupling optics. One way to suppress laser penetration is to design a double cladding fiber coupler, where one end of the coupler is fusion-spliced to a single-mode fiber that matches the core of the double cladding fiber.

6. Conclusions

A versatile, compact, catheter-like, two-photon endoscope was constructed for imaging of tissues. The probe clearly visualized the aqueous outflow pathway, including the trabecular meshwork, of fixed human eyes, indicating its feasibility for real-time investigation. The probe consists of a double cladding fiber, a piezoelectric driven fiber scanner, and an assembly of three achromatic doublet lenses. With the introduction of the doublet micro-lenses, the endoscope has not only micron-level spatial resolution but also significantly reduced chromatic effects, which enhance its fluorescence signal collection efficiency. Selection of an appropriate fiber and methods for reducing image distortion are discussed in detail. Delicate control of the drive signals was demonstrated to be a simple but effective method to suppress the image distortions that are intrinsically associated with resonant fiber scanner based imaging devices.

Acknowledgments

The authors wish to thank Mr. Don Rippon for assistance in construction of electronic circuitry and Mr. Francisco Tobias for design and construction of mechanical components. Support by the National Institutes of Health (NIH) under grant no. EY018318-01A1 is gratefully acknowledged.